

<https://doi.org/10.1038/s41699-025-00611-y>

# Origin of large variations of current on/off ratio and switching voltage in atomically thin memristors: an exascale ab initio transport study

Check for updates

Liangbo Liang<sup>1</sup> ✉, Wenchang Lu<sup>2</sup>, Jameela Fatheema<sup>3</sup>, Emil Briggs<sup>2</sup>, Deji Akinwande<sup>3</sup>, Jerzy Bernholc<sup>2</sup> & Panchapakesan Ganesh<sup>1</sup>

Nonvolatile resistive switching in two-dimensional monolayers opens a new avenue for high-density memory/computing devices. However, questions remain as to why the current on/off ratio and switching voltage vary significantly among different devices. Here, we simulate electronic transport of large systems consisting of a h-BN monolayer sandwiched by gold electrodes, enabled by an implementation of the nonequilibrium Green's function method in the exascale density functional theory (DFT) code: Real-space MultiGrid. Systematic calculations reveal that the wide range of on/off ratios is due to variations in interface distances between the electrode and h-BN that significantly modulate their wavefunction overlap. In addition, DFT calculations demonstrate that the energy barrier of a gold atom dissociating from the electrode to h-BN increases dramatically with the interface distance, thereby explaining the strong dependence of the switching voltage on distance. Our work demonstrates the significance of interface distance in governing the current on/off ratio and switching voltage.

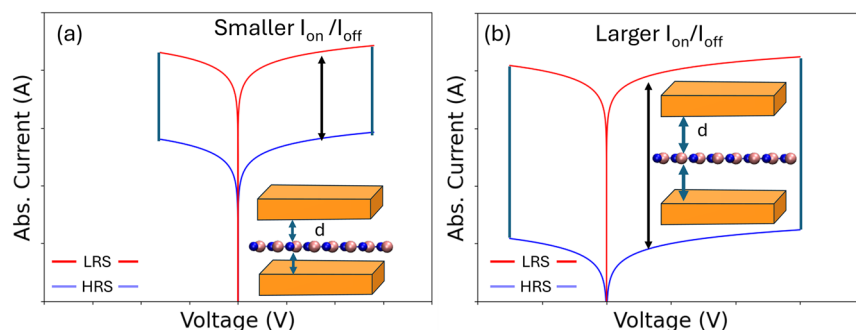
Two-dimensional (2D) layered materials, such as graphene, transition metal dichalcogenides, and hexagonal boron nitride (h-BN), have been intensively studied owing to their fundamental properties and technological potential. They have been explored for a variety of applications such as field-effect transistors, optoelectronics, flexible electronics, etc<sup>1–5</sup>. More recently, 2D materials show great promise in memristors, where nonvolatile resistive switching occurs between a high-resistance state (HRS) and a low-resistance state (LRS)<sup>6–19</sup>. In particular, memristor devices based on monolayer structures such as MoS<sub>2</sub> and h-BN in the vertical metal–insulator–metal configuration have attracted ever-growing attention because of their potential for developing high-density memory and computing devices at the ultrathin scale<sup>15,16,20–30</sup>. These atomically thin memristors are also known as atomristors<sup>15</sup>. Furthermore, 2D memristors or atomristors can also be used as artificial synapses for next-generation neuromorphic computing<sup>31–33</sup>.

To fully realize the technological potential of single-layer 2D material-based memristors, however, we must first understand the resistive switching mechanism. Numerous experimental and theoretical works by us and others<sup>15,16,22,23,27,34–36</sup> suggested that metal atoms are dissociated from the electrodes under a bias voltage and then adsorbed

on the sites of defects (vacancies and/or grain boundaries) in 2D monolayers, leading to the formation of metal conductive bridges and filaments between the electrodes and the 2D active layer, and subsequently a HRS to LRS transition. Different resistance states arise from different numbers of metal atoms in the interface for the conduction. The desorption of metal atoms from the defective sites under a reversed voltage and/or Joule heating returns the system to the original HRS. Nevertheless, there are still some open questions: why are the current on/off ratio and switching voltage, key metrics of memristors, strongly device-dependent in the same experiments? Why do they also vary significantly among different experiments? For example, for monolayer h-BN-based memristors, Wu et al.<sup>16</sup> found significant differences for the on/off ratio and switching voltage in crossbar devices with the same lateral area of  $2 \times 2 \mu\text{m}^2$ . Some devices attain the current on/off ratio around  $0.3 \times 10^5$  and the switching voltage about 2.0 V; in contrast, others possess substantially higher on/off ratio (up to  $10^7$ ) but also significantly higher switching voltage of  $\sim 3.4 \text{ V}$ <sup>16</sup>. Similar trends were reported for monolayer MoS<sub>2</sub>-based memristors using gold/graphene as the top electrode and gold as the bottom electrode, where the on/off ratio

<sup>1</sup>Center for Nanophase Materials Sciences, Oak Ridge National Laboratory, Oak Ridge, TN, USA. <sup>2</sup>Department of Physics, North Carolina State University, Raleigh, NC, USA. <sup>3</sup>Microelectronics Research Center, The University of Texas at Austin, Austin, TX, USA. ✉e-mail: [liangl1@ornl.gov](mailto:liangl1@ornl.gov)

**Fig. 1 | Schematic illustration of the hypothesis for memristor devices based on monolayer h-BN, where we proposed that large variations in the current on/off ratio and switching voltage are influenced by the electrode-BN distance  $d$ .** **a** For devices with shorter interface distances, they have lower current on/off ratios and lower switching voltages. **b** For devices with larger interface distances, they show higher current on/off ratios and higher switching voltages. Note that the interface (electrode-to-electrode) distance is  $2d$ .



can be as low as 1.6 and as high as  $10^7$ , and the switching voltage is modulated between 3.0 and 4.0 V<sup>15,37</sup>. Such strong variations of the switching ratio and voltage have not been thoroughly investigated yet, casting doubt on the resistive switching mechanism proposed in the literature and hindering reliable fabrication of 2D memristors at both laboratory and industrial scales. Although defect density has been found to affect the on/off ratio, the resulting variation of the ratio is less than one order of magnitude<sup>37,38</sup>. Therefore, we hypothesize that the interface distance plays a more crucial role for the significant variations of the switching ratio and voltage among devices<sup>15,16,21,22,37</sup>. Our hypothesis is schematically illustrated in Fig. 1: the devices in the left panel have cleaner interfaces and shorter interface distances so they have lower current on/off ratios and lower switching voltages; on the other hand, the devices in the right panel have residues at the interface, thus larger interface distances leading to higher current on/off ratios and higher switching voltages.

To test our hypothesis, simulating the electronic transport and directly computing  $I$ - $V$  curves of the memristors using ab initio approaches is necessary. Although several prior works have carried out such simulations<sup>23,34,35,37</sup>, neither of them considered different interface conditions and distances, induced by fabrication processes, to understand the large variations of the switching ratio and voltage. Additionally, the device sizes were usually limited due to the high computational cost of quantum transport simulations. In some cases, some layers of the gold electrodes had to be reduced to Au diploids to reduce the cost<sup>34,35</sup>. Such simplification probably made the calculated on/off ratios less accurate. In this work, by implementing the nonequilibrium Green's function (NEGF) method in a highly scalable first-principles density functional theory (DFT) code, the Real-space MultiGrid (RMG)<sup>39-42</sup>, we can directly simulate electronic transport of a h-BN monolayer sandwiched by top and bottom gold electrodes consisting of  $\sim 1000$  atoms (close to 8000 orbitals). Note that our transport simulations can be applied to larger supercell structures and multilayer 2D systems with several thousands of atoms<sup>43,44</sup>. In fact, the largest system we simulated in this work contains more than 3600 atoms. For each system with the size of  $\sim 1000$  atoms, the transport simulations need less than 3 h using 16 GPU nodes in the exascale supercomputer "Frontier" at Oak Ridge National Laboratory. Such speed and efficiency allow us to carry out systematic transport simulations at a variety of resistance states and interface distances. We found that the interface distance is a key factor affecting the current on/off ratio, which provides the first quantitative evidence on why the ratio can vary from  $10^0$  to  $10^7$  among different memristor devices. The calculated on/off ratio exhibits exponential dependence on the electrode-electrode distance, increasing by a factor of  $\sim 7.2$  per angstrom. In addition, DFT calculations demonstrate that the energy barrier of a gold atom dissociating from the Au electrode to bind with h-BN increases dramatically with the interface distance, thereby shedding light on the strong dependence of the switching voltage on the distance. Our results underscore the significance of the interface distance in governing the current on/off ratio and switching voltage and help to reconcile the inconsistencies between different samples and experimental groups. The

results presented here improve the understanding of the resistive switching mechanism in atomically thin memristors, also called atomristors, and provide valuable guidelines for engineering and optimizing memristor devices.

## Results

To understand why and how the current on/off ratios of the atomically thin memristors show significant variations among different experimental works<sup>15,16,37</sup> and even among different devices in the same works<sup>15,16</sup>, we simulated the electronic transport in a realistic Au/h-BN/Au device geometry using the self-consistent NEGF method implemented in RMG (more details in Methods) at a variety of resistance states and interface distances. According to prior experimental and theoretical works<sup>16,26,27,34</sup>, single boron vacancy on h-BN is the most plausible defect type to interact with metal atoms dissociated from the electrodes for enabling memristive switching. Therefore, we introduced a boron vacancy in h-BN and considered Au atom adsorption on the vacancy site, as shown in Fig. 2. Note that the equilibrium distance between h-BN and the Au (111) surface under an ideal condition (i.e., clean interface) is about 3.20 Å; however, for realistic devices, the fabrication process commonly involves polymers and solvents such as polydimethylsiloxane (PDMS), polymethyl methacrylate (PMMA), and de-ionized water<sup>15,16,37</sup>, which can introduce contaminants into the interface between the electrodes and h-BN, thereby leading to electrode-BN distances larger than 3.20 Å. Due to the surface roughness of the electrodes and the non-uniform presence of contaminants inside the interface, it is difficult to pinpoint the electrode-BN distance; in fact, the distance probably varies from location to location across the interface. The wavefunction overlap between the electrodes and h-BN is distance-dependent, affecting the transport. Therefore, we considered a wide range of electrode-BN distances from 3.20 to 7.50 Å. The lower bound of 3.2 Å corresponds to the equilibrium separation between monolayer h-BN and the Au(111) surface when no chemical residues exist between them. When fabrication-induced residues become trapped at the interface, the electrode-BN distance can be expressed as  $d = d(\text{residues-BN}) + d(\text{residues-electrode}) + t(\text{residues})$ , where  $d(\text{residues-BN})$  is the equilibrium separation distance between the residues and h-BN, and  $d(\text{residues-electrode})$  is the distance between the residues and the electrode surface. They are usually around 2.9–3.3 Å, the typical distance for physical (vdW type) interactions.  $t(\text{residues})$  is the thickness of the residues, which can vary from almost zero to several angstroms depending on the orientation relative to h-BN. Therefore, the electrode-BN distance can reach 6 Å and higher. We chose 7.5 Å as the upper-bound testing example to illustrate the effect of the electrode-BN distance. It can be higher in real devices, as will be discussed below based on experimental atomic force microscopy measurements of the step height of the h-BN monolayer after transfer on the substrate.

### The impact of the electrode-BN distance on the electronic transport

Figure 2a illustrates the atomic structure of the Au/h-BN/Au device at the equilibrium electrode-BN distance of 3.20 Å. According to our calculations,

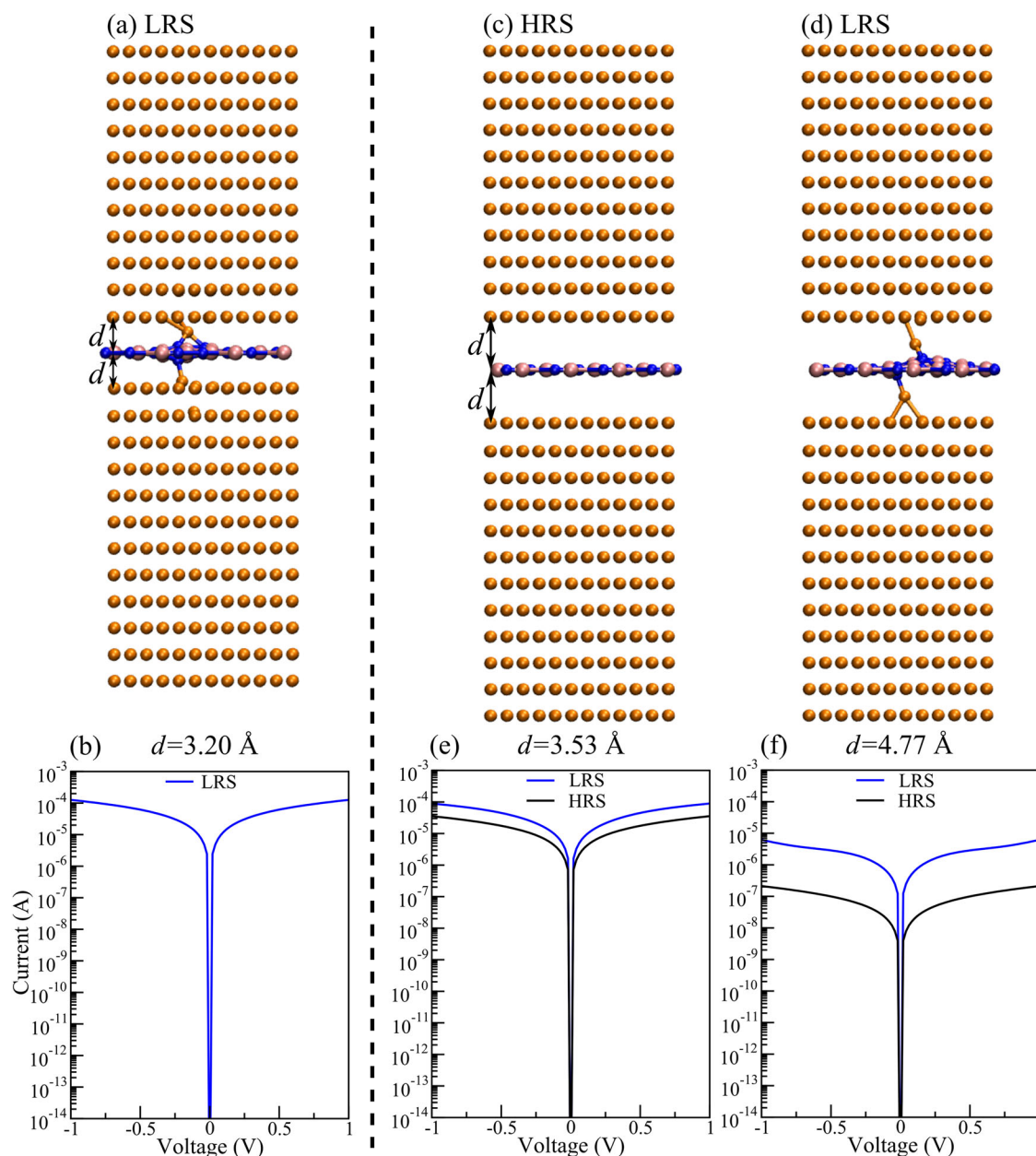


**Fig. 2 | Electronic transport simulations at short electrode-BN distances.**

**a** Atomic structure of the Au/h-BN/Au device at the equilibrium electrode-BN distance of 3.20 Å. Due to a boron vacancy in h-BN, an Au atom spontaneously moves towards the B vacancy to act as a conductive bridge, so the system is set to low-resistance state (LRS). **b** Calculated  $I$ - $V$  curve of the device at the LRS at the

3.20 Å distance. At a distance of 3.53 or 4.77 Å, the device assumes either a high-resistance state (HRS) shown in (c) or LRS in (d), depending on the atomic configurations. Calculated  $I$ - $V$  curves under different states at a distance of e 3.53 Å and f 4.77 Å. Here, the switching behavior at the SET/RESET voltage is not simulated. The device area in one unit cell is 2.62 nm<sup>2</sup>.

during the structural relaxation, an Au atom spontaneously moves towards the B vacancy site. It sits between the Au surface and h-BN, forming bonds with both the Au surface and h-BN, and acting as a conductive bridge between them. Consequently, the system is stuck in an LRS with or without an electric bias. For such a state, we computed its  $I$ - $V$  curve at various source-drain biases by calculating the current from the transmission spectrum using the Landauer formula<sup>45,46</sup>, as shown in Fig. 2b. Because the system remains in the LRS, there is no hysteresis during the  $I$ - $V$  sweep. However, when the electrode-BN distance is increased to 3.53 Å, the interaction between the Au surface and h-BN is weakened so that no gold atom is spontaneously displaced from the electrode. Therefore, without the application of an electric voltage, the system stays in an HRS, as shown in Fig. 2c. The application of a critical voltage enables a gold atom to dissociate from the electrode and subsequently be adsorbed on the vacancy site. In

such an electrode-BN distance, the gold atom bonds both with the Au surface and h-BN, leading to a conductive bridge illustrated in Fig. 2d. As demonstrated previously<sup>34</sup>, an Au atom can pass through h-BN via the boron vacancy, so a full conductive filament from the top to the bottom electrode is eventually formed, leading to a transition to the LRS in Fig. 2d. Figure 2e shows the simulated  $I$ - $V$  curves at both resistance states for the electrode-BN distance of 3.53 Å. The LRS exhibits a larger current than the HRS at any voltage, indicating higher conductance (lower resistance) due to the conductive filament across the interface. However, because the electrode-BN distance of 3.53 Å still allows considerable wavefunction overlap between the Au surface and h-BN, tunneling of electrons through the interface in the HRS is relatively easy, and thus, the resistance of the HRS is not notably higher than that of the LRS. As a result, the current on/off ratio near zero voltage (0.1 V) is only 2.29, and the hysteresis during the  $I$ - $V$

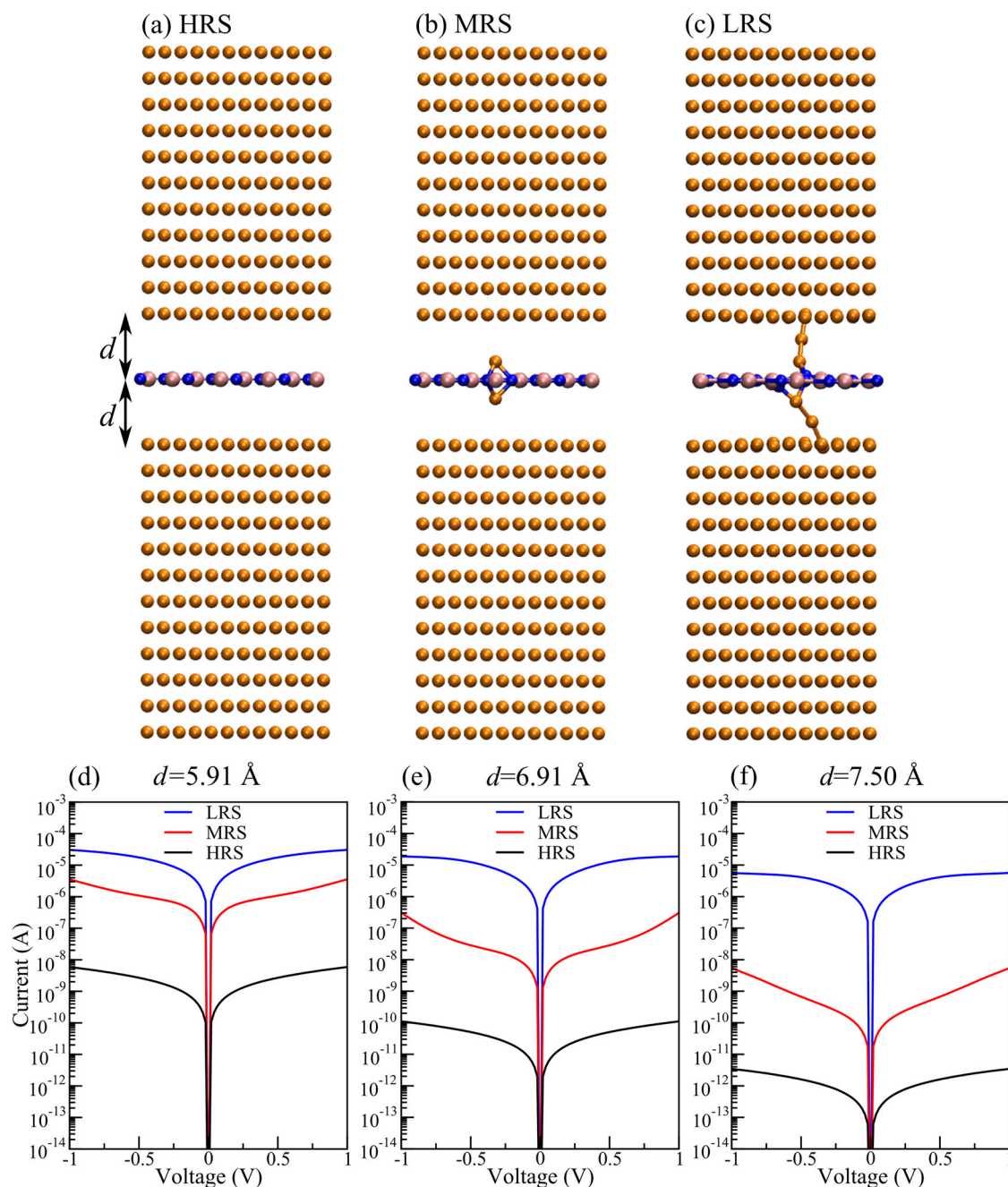


**Fig. 3 | Electronic transport simulations at relatively large electrode-BN distances.** Atomic structures of the Au/h-BN/Au device under different resistance states: **a** high-resistance state (HRS), **b** medium resistance state (MRS), and **c** low-resistance state (LRS). Calculated  $I$ - $V$  curves under different states at varying

electrode-BN distances: **d** 5.91 Å, **e** 6.91 Å, and **f** 7.50 Å. Here, the switching behavior at the SET/RESET voltage is not simulated. The device area in one unit cell is 2.62 nm<sup>2</sup>.

sweep in Fig. 2e is not significant. In short, if the distance is larger than the equilibrium one but not large enough to eliminate the wavefunction overlap between the electrode and the 2D monolayer, resistive switching can occur, albeit with relatively small current on/off ratios. This could be the reason why the switching ratios in monolayer MoS<sub>2</sub> memristors studied by Papadopoulos et al.<sup>37</sup> were not higher than 1.70. To enhance the current on/off ratio, we need to increase the electrode-BN distance to minimize the interactions between the electrode and h-BN (i.e., reduce the current leakage). Our simulations suggest that the HRS has much higher resistance than the LRS when the electrode-BN distance is increased to 4.77 Å, leading to a current on/off ratio of 31.93 and appreciable hysteresis during the  $I$ - $V$  sweep, as shown in Fig. 2f. Nevertheless, this ratio is still drastically lower than those (10<sup>4</sup> to 10<sup>7</sup>) reported by Wu et al.<sup>16</sup> for monolayer h-BN devices.

The increase in the on/off ratio with electrode-BN distance suggests that at even larger distances, the experimentally observed on/off ratios might be observed. Note that the OFF current at the HRS shown by the black curves in Figs. 2 and 3 corresponds to the quantum tunneling current.

Multiple resistance states occur when the electrode-BN distance is increased further to 5.91 Å in Fig. 3a. As illustrated in Fig. 3b, the adsorption of a single gold atom on the vacancy site no longer ensures a conductive bridge across the interface since the shortest separation distance between the bound Au atom and any gold atom from the electrode is more than 4.3 Å. Thus, the electronic transport falls back into the quantum tunneling regime<sup>27</sup>. However, compared to the HRS in Fig. 3a, its electrical resistance is still lower and thus is denoted as a medium resistance state (MRS). Clearly, an additional gold atom is needed to form a complete conductive filament

and generate the LRS, as demonstrated in Fig. 3c. The calculated  $I$ - $V$  curves of all three states are shown in Fig. 3d, where the  $I$ - $V$  curve of the MRS is between those of the HRS and LRS. For the distance of 5.91 Å, the current on/off ratio of MRS/HRS is around  $0.60 \times 10^3$ , while the ratio of LRS/HRS is computed to be  $0.68 \times 10^4$  (Table 1), indicating that the LRS resistance is about one order of magnitude lower than that of the MRS. As we continue to increase the electrode-BN distance, the tunneling barrier from the electrode to h-BN is getting higher for the HRS in Fig. 3a, so is the tunneling barrier from the electrode to the gold atom bound on h-BN in Fig. 3b. Since the current tends to decay exponentially with the vacuum distance, the HRS and MRS currents are continuously and substantially reduced when the electrode-BN distance grows from 5.91 Å to 6.91 Å to 7.50 Å, as shown in Fig. 3e, f. In contrast, for the LRS, the presence of a conductive filament across the interface guarantees current flow, so the current does not decrease considerably with distance. As a result, the current on/off ratio of LRS/HRS quickly climbs to  $0.22 \times 10^6$  for 6.91 Å and  $0.26 \times 10^7$  for 7.50 Å (Table 1). On the other hand, as the distance increases, quantum tunneling dominates the electronic transport in the MRS as well, and hence, the difference between the MRS and HRS gets smaller. This is reflected in the on/off ratio of MRS/HRS, as it does not increase from 5.91 Å to 7.50 Å (Table 1). In short, our simulations clearly show that the current on/off ratio between the LRS and HRS is strongly dependent on the electrode-BN distance and can vary between  $10^3$  and  $10^7$ , just like the experimental results reported by Wu et al.<sup>16</sup> Note that at an electrode-BN distance of 7.50 Å, the current on/off ratio is  $0.26 \times 10^7$ . Because the on/off ratio increases dramatically with the distance, it can exceed  $10^7$  when the distance is larger than 7.50 Å. According

to the fitting formula discussed below, it will exceed  $10^7$  when the distance is around 7.71 Å.

To gain a deeper understanding of the effects of the electrode-BN distance on memristor switching, we computed the zero-voltage electrical resistance at different resistance states as a function of the electrode-BN distance (Fig. 4a). For the HRS, where quantum tunneling is the dominant transport mechanism, the resistance clearly grows exponentially with the electrode-BN distance (the resistance  $R$  shown by black squares is plotted in the log scale, and  $\log(R)$  is almost linearly dependent on the distance  $d$ ). Since the current is proportional to the inverse of the resistance, the OFF current at the HRS decreases exponentially with the distance, as shown by black squares in Fig. 4b (log scale). For the MRS, as we discussed above, it corresponds to the adsorption of a single gold atom at the vacancy site of h-BN. When the electrode-BN distance  $d < 5$  Å (Fig. 2), this gold atom can form bonds with both the Au surface and h-BN, and thus act as a conductive bridge between them for electrons flowing across the interface. However, when  $d > 5$  Å (Fig. 3b), a single Au atom no longer ensures a conductive bridge across the interface, since the separation between the bound Au atom and the electrode is more than 4.3 Å. Thus, the electronic transport falls back into the quantum tunneling regime, and the tunneling begins to dominate as  $d$  continues to increase. As a result, for the MRS (shown by red triangles in Fig. 4a), the resistance  $R$  vs  $d$  follows two distinct patterns. When  $d > 5$  Å,  $R$  grows more rapidly with  $d$  due to quantum tunneling, similar to the tunneling in the HRS, and therefore the difference between MRS and HRS gets smaller (hence the current on/off ratio of MRS/HRS decreases as shown in Table 1). We note that when  $d < 5$  Å (Fig. 2), a single gold atom can form a conductive chain across the interface, and thus the MRS is the same as the LRS. For the LRS at  $d > 5$  Å, on the other hand, an additional gold atom is needed to form the complete conductive chain (Fig. 3c) to ensure electrons flow through the interface. For the LRS (blue stars in Fig. 4a), regardless of the electrode-BN distance, the resistance only mildly increases with  $d$  because electrons can directly flow from the top to the bottom electrodes. Consequently, the ON current at the LRS does not change much with the distance, as shown by blue stars in Fig. 4b. With the OFF current at the HRS decreasing exponentially with the distance (black squares in Fig. 4b), the current on/off ratio of LRS/HRS therefore increases exponentially with the distance following a fitting formula of  $y = A \times e^{B \times d}$ , where the coefficients  $A$  and  $B$  are  $5.94e-07$  (no unit) and  $3.95$  (in the unit of Å<sup>-1</sup>), respectively, as shown in Fig. 4c (the on/off ratio is also on the log scale). According to the fitting formula, the on/off ratio grows by a factor of  $\sim 7.2$  when the electrode-electrode distance is increased by one angstrom (i.e., the electrode-BN

**Table 1 | Calculated current on/off ratios of the Au/h-BN/Au device between medium resistance state (MRS) and high-resistance state (HRS), and between low-resistance state (LRS) and HRS at different distances**

Electrode-BN distance (Å)	On/off ratio (MRS/HRS)	On/off ratio (LRS/HRS)
3.53	2.29	2.29
4.77	31.93	31.93
5.91	$0.60 \times 10^3$	$0.68 \times 10^4$
6.91	$0.65 \times 10^3$	$0.22 \times 10^6$
7.50	$0.29 \times 10^3$	$0.26 \times 10^7$

For the distances of 3.53 and 4.77 Å, the MRS is the same as the LRS.

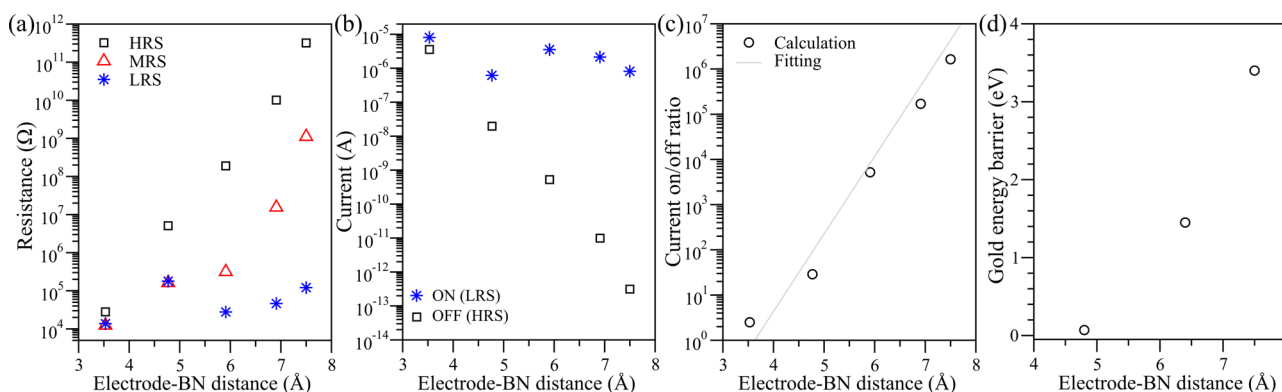


**Fig. 4 | Device parameters as a function of the electrode-BN distance.** **a** Calculated resistances of different states as a function of the electrode-BN distance for the Au/h-BN/Au device. Note that at shorter distances ( $< 5$  Å) the MRS is the same as the LRS (thus their data points are overlapped), while at larger distances ( $> 5$  Å) the MRS is no longer equivalent to the LRS. **b** Calculated ON and OFF currents near zero voltage (0.1 V) as a function of the electrode-BN distance. The OFF current corresponds to the HRS, while the ON current corresponds to the LRS. The device area in one unit cell is  $2.62 \text{ nm}^2$ . Calculated OFF (i.e., quantum tunneling) current density is shown in

Fig. S1 in Supplementary Information. **c** The corresponding current on/off ratio as a function of the electrode-BN distance. Gray line is a fitting curve based on the formula of  $y = A \times e^{B \times d}$ . The on/off ratio is basically defined between the LRS and HRS at any given distance. The Y axis is in the log scale in (a-c). Note that the interface (electrode-to-electrode) distance is twice the electrode-BN distance. **d** Calculated energy barrier of an Au atom dissociated from the Au electrode to adsorbing on the B vacancy site of the h-BN surface as a function of the electrode-BN distance.

**Table 2 | Summary of measured current on/off ratio and switching voltage in experimental 2D monolayer memristors based on different transfer techniques and metal electrodes**

Active layer	Polymer transfer	Electrodes (device area)	On/off ratio	Switching voltage (V)	Reference
h-BN	PMMA	Au/Au (0.5 × 0.5 μm <sup>2</sup> )	~0.5 × 10 <sup>5</sup>	~1.4	21
h-BN	PMMA	Au/Au (1 × 1 μm <sup>2</sup> )	~10 <sup>5</sup>	~2.2	22
h-BN	PMMA	Au/Au (1 × 1 μm <sup>2</sup> )	median: ~0.25 × 10 <sup>7</sup>	median: ~3.3	16
h-BN	PMMA	Au/Au (2 × 2 μm <sup>2</sup> )	~0.3 × 10 <sup>5</sup> –10 <sup>7</sup> (median: ~0.2 × 10 <sup>6</sup> )	~2.0–3.4 (median: ~2.8)	16
h-BN	PMMA	Au/Au (10 × 10 μm <sup>2</sup> )	median: ~100	median: ~1.0	16
MoS <sub>2</sub>	dry transfer	Au/graphene/Au (2.4 × 2.4 μm <sup>2</sup> )	~1.6	~3.0	37
MoS <sub>2</sub>	PDMS	Au/graphene/Au (1 × 1 μm <sup>2</sup> )	~10 <sup>7</sup>	~4.0	15
MoS <sub>2</sub>	PDMS	Au/Au (1 × 1 μm <sup>2</sup> )	median: ~10 <sup>7</sup>	median: ~3.4	15
MoS <sub>2</sub>	PDMS	Au/Au (2 × 2 μm <sup>2</sup> )	median: ~0.3 × 10 <sup>6</sup>	median: ~1.0	15
MoS <sub>2</sub>	PDMS	Au/Au (100 × 100 μm <sup>2</sup> )	median: ~10	median: ~0.5	15

For some devices, only median values are reported in the experimental works, as shown in the table.

distance  $d$  is increased by a half angstrom). To summarize, our simulations demonstrate that the resistance of the HRS and the resulting OFF current and on/off ratio exhibit exponential dependence on the electrode-BN distance, thereby leading to substantial variations in the on/off ratio between 10<sup>0</sup> and 10<sup>7</sup>. Note that the absolute values of calculated OFF current in Fig. 4b and OFF current density in Fig. S1 (i.e., quantum tunneling current and current density) cannot be directly compared to the values in experimental devices for multiple reasons. First, a flat gold surface is considered in the calculations, but the gold electrodes in experiments have surface roughness, leading to variations in the distance between the electrode surface and h-BN. Second, due to chemical residues inside the interface, the electrode-BN distance in experimental devices could be notably larger than the equilibrium one (~3.20 Å). Since the tunneling current decays exponentially with the electrode-BN distance, different distances between the calculations and experiments can lead to different currents by orders of magnitude. For example, when the electrode-BN distance is increased from 3.53 Å to 4.77 Å, the OFF current is reduced by more than two orders of magnitude. Finally, because the electronic band gap of h-BN is underestimated by the calculations, the transport simulations usually overestimate the tunneling current compared to experiments. In short, caution needs to be taken when comparing the tunneling current and current density (similarly, resistance) between the calculations and experiments. In this work, the physical trends of the calculated resistance, current, and on/off ratio versus the electrode-BN distance are more reliable than the absolute values.

### The impact of the electrode-BN distance on the switching voltage

It is interesting to note that the distance between the h-BN active layer and the Au electrode significantly affects the energy barrier of the dissociation of an Au atom from the electrode to be adsorbed on the vacancy site in h-BN. Using the climbing image nudged elastic band (NEB) method<sup>47</sup>, we calculated the energy barrier when the electrode-BN distance varies from 7.5 to 6.4 to 4.8 Å and found out that it is dramatically lowered from 3.40 to 1.45 to 0.07 eV, as shown in Fig. 4d. When the Au atom dissociates from the electrode, its orbitals become unsaturated, and it becomes energetically less stable unless it forms new bonds with other atoms to lower its energy. The shorter the distance between the electrode and h-BN, the quicker new bonds are formed between the Au atom and h-BN, thereby lowering the energy barrier. Detailed discussions about the NEB calculations, gold migration pathways, and the NEB energy profiles can be found in the Supplementary Information. These energy barriers are extracted from the full NEB reaction coordinates plotted in Fig. S2. The NEB pathway involves a single gold atom transitioning from its initial state (adsorbed within the bulk-like electrode surface) to the final state (bound at the boron vacancy site in the h-BN). Representative atomic structures and the energies of the initial, transition, and final states for each electrode-BN distance are shown in Fig. S3. Because

the electrode-BN distance varies from device to device during the fabrication process, the energy barrier and subsequently the switching voltage (i.e., SET voltage) vary strongly in h-BN devices even with the same lateral area<sup>16</sup>.

### Comparison between calculations and experiments

Now, we are ready to connect our simulation results (Table 1 and Fig. 4) to experimental findings in the literature that are summarized in Table 2. For typical crossbar h-BN devices, the fabrication processes involve polymers and solvents such as PMMA, ammonia persulfate solution, de-ionized water, and acetone, which inevitably introduce polymer residues and contaminants into the interface<sup>16,21,22</sup>. In combination with the surface roughness of the electrodes, the electrode-BN distance is therefore considerably larger than the equilibrium distance of 3.20 Å, leading to current on/off ratios higher than 10<sup>4</sup> as shown in Table 2. Furthermore, the distance varies from device to device since the amount of chemical residues inside the interface fluctuates during the fabrication process of each device, resulting in strong variations of the on/off ratio between 10<sup>4</sup> and 10<sup>7</sup> (Table 2) in the same experimental work<sup>16</sup> and among different works<sup>16,21,22</sup>. Following the same logic, the switching voltage is also strongly modulated between 1.4 and 3.4 V<sup>16,21,22</sup>. Regarding the distance's variation due to fabrication residues and electrodes' surface roughness, cross-sectional transmission electron microscopy (TEM) is a great tool to image the interface. However, to the best of our knowledge, no cross-sectional TEM data have been provided to show unequivocally the interface spacing and its variation across the entire device. This matter is the subject of a future experimental work. What is known is that residues and electrodes' surface roughness inevitably increase the interface gap, and this can be seen indirectly in various atomic force microscopy (AFM) measurements of the step height of the h-BN monolayer after transfer but before top electrode deposition. After the transfer of the h-BN monolayer on a substrate, the measured step height relative to the substrate has been reported in a wide range from 4.9 Å (average value)<sup>16</sup> to 5.8 ± 0.6 Å<sup>48</sup> to 6.9 Å<sup>27</sup> to 8 ± 1 Å (the root-mean-square (RMS) roughness is 5.8 Å)<sup>49</sup>. The step height's variation among different experimental works and the large RMS roughness relative to the film thickness found in ref. 49 have been commonly attributed to entrapped water and polymer residues introduced during the transfer. Gorbachev et al.<sup>50</sup> reported that the h-BN films are often lifted above the substrate by up to extra 10 Å due to residues. Therefore, the electrode-BN distances ranging from 3.20 to 7.50 Å considered in our calculations should be realistic. In addition to the electrode-BN distance, it is important to note that the device area, the junction (or overlap) area between the top and bottom electrodes, can also strongly affect the on/off ratio and switching voltage<sup>51</sup>. Both decrease as the device area increases, as shown in Table 2<sup>15,16</sup>. For h-BN devices, when the device area is increased from 1 × 1 μm<sup>2</sup> to 2 × 2 μm<sup>2</sup>, the median value of the on/off ratio is reduced by one order of magnitude, from ~0.25 × 10<sup>7</sup> to ~0.2 × 10<sup>6</sup>, but it is dramatically decreased to ~100 when the area reaches

$10 \times 10 \mu\text{m}^2$ <sup>16</sup>. For MoS<sub>2</sub> devices, when the device area is increased from  $1 \times 1 \mu\text{m}^2$  to  $2 \times 2 \mu\text{m}^2$ , the current on/off ratio is reduced by a factor of 33, from  $\sim 10^7$  to  $\sim 0.3 \times 10^6$ <sup>15</sup>, but it is dramatically lowered to 10 when the area reaches  $100 \times 100 \mu\text{m}^2$ . Therefore, the study of device variability requires the device areas to be as close as possible. The device variation is not significant with area changes from  $1 \times 1 \mu\text{m}^2$  to  $2 \times 2 \mu\text{m}^2$ . Consequently, in Table 2 we compared the h-BN devices from three experimental works<sup>16,21,22</sup> with device areas of  $0.5 \times 0.5$ ,  $1 \times 1$ , and  $2 \times 2 \mu\text{m}^2$ , which are not too different, to ensure that the device variations are mainly due to the interface condition and distance, not the device area. In fact, smaller device areas in refs. 21. and<sup>22</sup> suggest that their on/off ratios and switching voltages should be further smaller if the devices were scaled up to  $2 \times 2 \mu\text{m}^2$  used in ref. 16. In other words, the lower limit of the on/off ratio and switching voltage should be probably close to  $10^4$  and 1.0 V, respectively, indicating an even wider variation range for h-BN memristors due to the interface distance. Similar analysis can be applied to MoS<sub>2</sub> devices. Reference<sup>37</sup> reported a current on/off ratio of  $\sim 1.6$  and a SET voltage of  $\sim 3.0$  V for monolayer MoS<sub>2</sub> memristors using mechanically exfoliated monolayer samples and a dry transfer technique that results in clean interfaces with shorter distances. According to our simulations, when the electrode-BN distance is close to the equilibrium one, the on/off ratio can be rather small and close to 1. In contrast, ref. 15 found a much higher on/off ratio of  $\sim 10^7$  and a larger SET voltage of  $\sim 4.0$  V for monolayer MoS<sub>2</sub> devices with the same electrodes, but using chemical vapor deposition grown samples and the PDMS-assisted transfer, which tends to leave chemical residues in the interface and leads to much larger electrode-BN distances. This can subsequently give rise to the substantially higher on/off ratio and switching voltage as demonstrated by the calculations shown in Table 1 and Fig. 4. Note that the device areas in refs. 37 and<sup>15</sup> do not differ much. As discussed above, when the device area is increased from  $1 \times 1 \mu\text{m}^2$  to  $2 \times 2 \mu\text{m}^2$ , the on/off ratio is slightly reduced from  $\sim 10^7$  to  $\sim 0.3 \times 10^6$  according to ref. 15. It is still  $\sim 10$  when the device area is substantially increased to  $100 \times 100 \mu\text{m}^2$ . Therefore, we expect that the on/off ratio for the device area of  $2.4 \times 2.4 \mu\text{m}^2$  in ref. 15 (not studied in this work) should be  $\sim 10^5$ , and at least much higher than 10. The dramatic reduction of the on/off ratio to only  $\sim 1.6$  for the device area of  $2.4 \times 2.4 \mu\text{m}^2$  in ref. 37 is thus not due to the device area. The effect of the device area can be ruled out as the leading cause of the observed variation in the ratio and the voltage.

Note that the systems are periodically repeated in our simulations, and in each unit cell, the in-plane cell size is  $1.51 \text{ nm} \times 1.74 \text{ nm}$ , so that the device area in one unit cell is  $2.62 \text{ nm}^2$ , which is relatively small. Due to the periodic boundary condition, one cannot simply conclude that the device area in simulations is  $2.62 \text{ nm}^2$  and the simulation results are limited to small-area devices. In experimental devices, the on/off ratio can change from  $10^7$  to 10 when the area is changed from  $1 \times 1 \mu\text{m}^2$  to  $100 \times 100 \mu\text{m}^2$ . Our simulations can produce such a ratio change when the electrode-BN distance varies from  $\sim 7.5$  to  $\sim 3.5 \text{ \AA}$ , while using the same unit cell size. We hypothesize that the effects of chemical residues in the interface are stronger in small devices. Chemical residues are broken into pieces randomly scattered on top and bottom of the 2D flake. For devices with a small lateral area, such as  $1 \times 1 \mu\text{m}^2$ , some large chemical residue molecules may fill the entire interface and thus push the vertical separation to higher values beyond  $7 \text{ \AA}$ , thereby leading to much higher on/off ratios and switching voltages according to our simulations. However, for devices with larger areas, such as  $100 \times 100 \mu\text{m}^2$ , the lateral area could be larger than any residue molecules, and thus the gap between two molecules constitutes a clean interface region with a shorter separation distance. As the device area becomes larger, the area with a shorter interface distance gets larger and begins to dominate the transport. Due to a shorter distance, the switching will occur at these locations first since the switching voltage is lower there. In short, a larger surface area of the electrode would reduce the effect of chemical residues and increase the likelihood of a shorter interface distance at some contact points, contributing to the decrease of the on/off ratio and the switching voltage according to our simulations. Therefore, our simulation results could work for both large and small device areas. The results are not limited by the lateral

area of the unit cell because we focus on the effect of the interface distance (in the vertical direction rather than the lateral direction). To verify our hypothesis, further experimental works need to be carried out. A direct experimental means is to make a variety of devices with different device areas using different processing methods and perform cross-sectional transmission TEM measurements to unequivocally measure the interface spacing and correlate this to experimental transport measurements. This will be future work for experimental research. An indirect and partial approach is to use conductive AFM<sup>52</sup> to scan the 2D monolayer surface after transfer on a substrate but before top electrode deposition, as mentioned above. By correlating the height with the tunneling current across the 2D surface, we could at least reveal the variation range of the distance between the AFM tip and the substrate and demonstrate how the OFF current depends on the distance.

Finally, we examined the effect of defect density on the current on/off ratio. In this work, without mentioning otherwise, the defect density in monolayer h-BN is  $0.38 \text{ nm}^{-2}$ . According to an experimental work on monolayer h-BN grown by chemical vapor deposition<sup>53</sup>, the defect concentration is in the range of  $0.03\text{--}0.30 \text{ nm}^{-2}$  (i.e.,  $0.03\text{--}0.30 \times 10^{14} \text{ cm}^{-2}$ ). To make the simulated defect concentration more comparable with experimental values, we have considered larger unit cell sizes and thus lower defect densities at an electrode-BN distance of  $\sim 6 \text{ \AA}$ , and summarized the calculated current on/off ratio versus the defect density in Table S1 in Supplementary Information. The largest Au/h-BN/Au unit cell contains more than 3600 atoms with a defect concentration of  $\sim 0.09 \text{ nm}^{-2}$ . Unfortunately, it is computationally prohibitive to simulate the experimental lower limit of the defect density ( $0.03 \text{ nm}^{-2}$ ), which requires more than 10,000 atoms. According to our simulations (Table S1), the current on/off ratio changes between  $0.30 \times 10^4$  and  $0.96 \times 10^4$  when the defect concentration grows from  $\sim 0.09$  to  $0.19$  to  $0.38 \text{ nm}^{-2}$ . Both our calculations and two prior experimental works<sup>37,38</sup> found that the on/off ratio variation by defect engineering is within one order of magnitude, and thus defects can also be ruled out as the primary cause for the substantial variations in the on/off ratio between  $10^0$  and  $10^7$ . Although the defect density used in our calculations for the effect of the interface distance is larger than the experimental values, the physical trends (i.e., strong dependence of the current on/off ratio and the switching voltage on the distance) still hold.

## Discussion

In summary, we have carried out electronic transport simulations in a realistic Au/h-BN/Au device geometry consisting of  $\sim 1000$  atoms using the DFT package RMG. The massive parallelization of the real-space DFT-NEGF method on exascale supercomputers allows us to systematically study memristor switching at a variety of interface distances for such large systems. We found that the current on/off ratio increases exponentially with the distance, largely due to the exponential increase in the HRS resistance and the exponential decrease in the OFF current with the vacuum thickness. According to our fitting formula, it grows by a factor of  $\sim 7.2$  when the electrode-electrode distance is increased by one angstrom. It can grow from  $10^0$  to  $10^7$  as the interface distance increases, which is a key contributing factor to the fact that the experimental on/off ratios vary significantly, in this same range, among different devices and experimental works. Furthermore, first-principles NEB calculations also revealed that the energy barrier for Au atom dissociation from the electrode increases dramatically with the interface distance, which explains why the switching voltage fluctuates strongly depending on the interface conditions and distances of the devices. Our work helps to reconcile the inconsistent results between the current on/off ratios among different works. It also provides a deeper understanding of the switching mechanism in atomically thin memristors and uncovers the crucial role of the interface distance in governing the current on/off ratio and switching voltage. Our simulations demonstrate that control of the interface distance is of great significance to ensure performance uniformity in practical memristive devices. Note that our device geometry is symmetric for the top and bottom electrodes, while it is probably asymmetric in terms of the distance and formation of filaments due to the random distribution of

chemical residues in the interface. This will be a subject of future study. In addition, besides the interface distance, the impact of different defects in the monolayer structures, such as grain boundaries<sup>51</sup>, will also need to be studied, which will be a subject of future work too. However, the exponential dependence of the current on/off ratio on the distance and the conclusions made in this work should not be affected by the device asymmetry and grain boundaries.

## Methods

### Structural relaxation and energy barrier calculations of a single Au/h-BN interface

First-principles DFT calculations were performed through the plane-wave Vienna Ab initio Simulation Package (VASP) software<sup>54</sup>. Electron-ion interactions were described by the projector-augmented-wave pseudo-potentials, and exchange-correlation interactions were described by the generalized gradient approximation using the Perdew-Burke-Ernzerhof functional<sup>55</sup>. For the interface between the Au electrode and monolayer h-BN, we constructed a commensurate hexagonal unit cell of h-BN with an Au (111) surface on the top, where there are 4 boron atoms, 4 nitrogen atoms, and 3 Au atoms per metal layer<sup>27,56</sup>. The most stable configuration corresponds to one Au atom on top of a boron atom, one Au atom on top of a nitrogen atom, and one Au atom on top of the center of a hexagon<sup>27</sup>. The Au (111) surface was simulated by four metal layers. The DFT-D3 method was adopted to capture the van der Waals interactions<sup>57</sup>. The system was modeled by a periodic slab geometry with a vacuum separation of 21 Å in the out-of-plane direction. Atoms were relaxed until the residual forces were below 0.01 eV/Å, and in-plane lattice constants were also optimized using the option of ISIF = 4 with the cutoff energy set at 520 eV. A  $k$ -point sampling of  $12 \times 12 \times 1$  was used. Based on the optimized hexagonal unit cell of Au (111)/h-BN, a  $3 \times 3 \times 1$  supercell was built, in which a boron vacancy was introduced to study the interactions between the Au electrode and the B vacancy. For the supercell structure, the outer two gold layers were fixed to mimic the bulk gold, while other atoms were relaxed until the residual forces were below 0.01 eV/Å. A single  $\Gamma$  point was used for the  $k$ -point sampling, and the cutoff energy was 400 eV. Such relaxation gives us the equilibrium separation distance between h-BN and the Au surface, which is around 3.2 Å. To model larger electrode-BN distances varying from 4.8 to 7.5 Å, we manually increased the separation distance to a given distance and fixed the  $z$  coordinates of atoms in the h-BN layer that are far away from the B vacancy, while still allowing atoms near the vacancy site in h-BN and the atoms in the inner two gold layers to move freely. The constrained structural optimization captured the atomic relaxation near the vacancy site while maintaining the electrode-BN distance at the given value. Finally, the climbing image NEB method was adopted to calculate the energy barrier for an Au atom dissociated from the electrode and migrated to the vacancy site on h-BN<sup>47</sup>. Four intermediate images along the reaction path were created for the NEB optimization to find the transition state and the energy barrier (the force criterion was set at 0.05 eV/Å).

### Structural relaxation and transport simulations of the Au/h-BN/Au device

To simulate the electronic transport of a realistic Au/h-BN/Au device, we built a large heterostructure where top and bottom Au electrodes sandwich the h-BN monolayer. This device configuration was constructed based on the commensurate hexagonal unit cell of h-BN with the Au (111) surface discussed above. However, here we introduced the Au (111) surface on both the top and bottom of the h-BN monolayer as the top and bottom Au electrodes, respectively. For the top electrode, there are 11 gold layers in total with an ABCABCABCAB order counting from the inner to outer layers (inner layers closer to h-BN); for the bottom electrode, there are 12 gold layers in total with an ABCABCABCABC order counting from the inner to outer layers (inner layers closer to h-BN). In this way, a periodic boundary condition can be naturally imposed in the out-of-plane direction. The lattice constants and atomic positions were optimized using

VASP until the residual forces were below 0.01 eV/Å. For the transport simulations, we converted the optimized hexagonal lattice to the orthorhombic lattice where the in-plane lattice constants are  $a = 5.017$  Å and  $b = 8.689$  Å, and then expanded the orthorhombic unit cell to a  $3 \times 2 \times 1$  supercell for which we introduced a boron vacancy in h-BN and considered Au atom adsorption on the vacancy site. In the supercell, only the innermost three gold layers are allowed to relax for both electrodes, while other layers are fixed to mimic the bulk gold. After structural relaxation via VASP (coordinate files of the full systems at different electrode-BN distances in the format of POSCAR are attached as Supplemental Information), the transport simulations were carried out based on the first-principles DFT code RMG<sup>39</sup> that has been massively parallelized in real space<sup>40</sup>, using its implementation<sup>42,58,59</sup> of the self-consistent nonequilibrium Green's function method<sup>60,61</sup>. Four optimally localized orbitals per atom were used for boron and nitrogen atoms, while nine orbitals per atom were employed for gold atoms. For all the atoms, the localized orbital radius was set to 8.5 Bohr. The localized orbitals for each subsystem (the Au leads and the center conductor part) were variationally optimized to have an optimal and accurate basis set<sup>42,58,59</sup>. The  $I$ - $V$  curves were obtained at various source-drain biases by calculating the current from the transmission spectrum using the Landauer formula<sup>45,46</sup>.

### Data availability

The data that support the plots within this paper and other findings of this study are available from the corresponding authors upon reasonable request.

### Code availability

Upon request, authors will make available any previously unreported computer code or algorithm used to generate results that are reported in the paper and central to its claims.

Received: 3 April 2025; Accepted: 18 September 2025;

Published online: 13 November 2025

## References

- Akinwande, D. et al. Graphene and two-dimensional materials for silicon technology. *Nature* **573**, 507–518 (2019).
- Wang, Q. H., Kalantar-Zadeh, K., Kis, A., Coleman, J. N. & Strano, M. S. Electronics and optoelectronics of two-dimensional transition metal dichalcogenides. *Nat. Nanotechnol.* **7**, 699–712 (2012).
- Akinwande, D., Petrone, N. & Hone, J. Two-dimensional flexible nanoelectronics. *Nat. Commun.* **5**, 5678 (2014).
- Lanza, M., Smets, Q., Huyghebaert, C. & Li, L.-J. Yield, variability, reliability, and stability of two-dimensional materials based solid-state electronic devices. *Nat. Commun.* **11**, 5689 (2020).
- Migliato Marega, G. et al. Logic-in-memory based on an atomically thin semiconductor. *Nature* **587**, 72–77 (2020).
- Sangwan, V. K. et al. Multi-terminal memtransistors from polycrystalline monolayer molybdenum disulfide. *Nature* **554**, 500–504 (2018).
- Li, D. et al. MoS<sub>2</sub> memristors exhibiting variable switching characteristics toward biorealistic synaptic emulation. *ACS Nano* **12**, 9240–9252 (2018).
- Sangwan, V. K. et al. Gate-tunable memristive phenomena mediated by grain boundaries in single-layer MoS<sub>2</sub>. *Nat. Nanotechnol.* **10**, 403–406 (2015).
- Kim, M. et al. Zero-static power radio-frequency switches based on MoS<sub>2</sub> atomistors. *Nat. Commun.* **9**, 2524 (2018).
- Zhao, H. et al. Atomically thin femtojoule memristive device. *Adv. Mater.* **29**, 1703232 (2017).
- Bessonov, A. A. et al. Layered memristive and memcapacitive switches for printable electronics. *Nat. Mater.* **14**, 199–204 (2015).
- Qian, K. et al. Hexagonal boron nitride thin film for flexible resistive memory applications. *Adv. Funct. Mater.* **26**, 2176–2184 (2016).

13. Pan, C. et al. Coexistence of grain-boundaries-assisted bipolar and threshold resistive switching in multilayer hexagonal boron nitride. *Adv. Funct. Mater.* **27**, 1604811 (2017).
14. Zhang, S. et al. Memristors based on two-dimensional h-BN materials: synthesis, mechanism, optimization and application. *npj 2D Mater. Appl.* **8**, 81 (2024).
15. Ge, R. et al. Atomristor: nonvolatile resistance switching in atomic sheets of transition metal dichalcogenides. *Nano Lett.* **18**, 434–441 (2018).
16. Wu, X. et al. Thinnest nonvolatile memory based on monolayer h-BN. *Adv. Mater.* **31**, 1806790 (2019).
17. Xu, R. et al. Vertical MoS<sub>2</sub> double-layer memristor with electrochemical metallization as an atomic-scale synapse with switching thresholds approaching 100 mV. *Nano Lett.* **19**, 2411–2417 (2019).
18. Wang, M. et al. Robust memristors based on layered two-dimensional materials. *Nat. Electron.* **1**, 130–136 (2018).
19. Li, X.-D. et al. Resistive memory devices at the thinnest limit: progress and challenges. *Adv. Mater.* **36**, 2307951 (2024).
20. Wu, X., Ge, R., Huang, Y., Akinwande, D. & Lee, J. C. Resistance state evolution under constant electric stress on a MoS<sub>2</sub> non-volatile resistive switching device. *RSC Adv.* **10**, 42249–42255 (2020).
21. Kim, M. et al. Analogue switches made from boron nitride monolayers for application in 5 G and terahertz communication systems. *Nat. Electron.* **3**, 479–485 (2020).
22. Ge, R. et al. A library of atomically thin 2D materials featuring the conductive-point resistive switching phenomenon. *Adv. Mater.* **33**, 2007792 (2021).
23. Hus, S. M. et al. Observation of single-defect memristor in an MoS<sub>2</sub> atomic sheet. *Nat. Nanotechnol.* **16**, 58–62 (2021).
24. Wu, X., Ge, R., Akinwande, D. & Lee, J. C. Understanding of multiple resistance states by current sweeping in MoS<sub>2</sub>-based non-volatile memory devices. *Nanotechnology* **31**, 465206 (2020).
25. Kim, M. et al. Monolayer molybdenum disulfide switches for 6 G communication systems. *Nat. Electron.* **5**, 367–373 (2022).
26. Yang, S. J. et al. Reconfigurable low-voltage hexagonal boron nitride nonvolatile switches for millimeter-wave wireless communications. *Nano Lett.* **23**, 1152–1158 (2023).
27. Yang, S. J. et al. Volatile and nonvolatile resistive switching coexistence in conductive point hexagonal boron nitride monolayer. *ACS Nano* **18**, 3313–3322 (2024).
28. Nikam, R. D., Rajput, K. G. & Hwang, H. Single-atom quantum-point contact switch using atomically thin hexagonal boron nitride. *Small* **17**, 2006760 (2021).
29. Yang, S. J. et al. Giant memory window performance and low power consumption of hexagonal boron nitride monolayer atomristor. *npj 2D Mater. Appl.* **9**, 9 (2025).
30. Li, Y. et al. Resistive switching properties of monolayer h-BN atomrisors with different electrodes. *Appl. Phys. Lett.* **120**, 173104 (2022).
31. Tang, J. et al. Bridging biological and artificial neural networks with emerging neuromorphic devices: fundamentals, progress, and challenges. *Adv. Mater.* **31**, 1902761 (2019).
32. Sangwan, V. K. & Hersam, M. C. Neuromorphic nanoelectronic materials. *Nat. Nanotechnol.* **15**, 517–528 (2020).
33. Huh, W., Lee, D. & Lee, C.-H. Memristors based on 2D materials as an artificial synapse for neuromorphic electronics. *Adv. Mater.* **32**, 2002092 (2020).
34. Li, X.-D., Chen, N.-K., Wang, B.-Q. & Li, X.-B. Conductive mechanism in memristor at the thinnest limit: The case based on monolayer boron nitride. *Appl. Phys. Lett.* **121**, 073505 (2022).
35. Li, X.-D., Wang, B.-Q., Chen, N.-K. & Li, X.-B. Resistive switching mechanism of MoS<sub>2</sub> based atomristor. *Nanotechnology* **34**, 205201 (2023).
36. Mitra, S. & Mahapatra, S. Atomistic description of conductive bridge formation in two-dimensional material based memristor. *npj 2D Mater. Appl.* **8**, 26 (2024).
37. Papadopoulos, S. et al. Ion migration in monolayer MoS<sub>2</sub> memristors. *Phys. Rev. Appl.* **18**, 014018 (2022).
38. Wu, X. et al. Electron irradiation-induced defects for reliability improvement in monolayer MoS<sub>2</sub>-based conductive-point memory devices. *npj 2D Mater. Appl.* **6**, 31 (2022).
39. Briggs, E. L., Sullivan, D. J. & Bernholc, J. Large-scale electronic-structure calculations with multigrid acceleration. *Phys. Rev. B* **52**, R5471–R5474 (1995).
40. Briggs, E. L., Sullivan, D. J. & Bernholc, J. Real-space multigrid-based approach to large-scale electronic structure calculations. *Phys. Rev. B* **54**, 14362–14375 (1996).
41. Briggs, E. L., Lu, W. & Bernholc, J. Adaptive finite differencing in high accuracy electronic structure calculations. *npj Comput. Mater.* **10**, 17 (2024).
42. Lu, W., Meunier, V. & Bernholc, J. Nonequilibrium quantum transport properties of organic molecules on silicon. *Phys. Rev. Lett.* **95**, 206805 (2005).
43. Tan, B., Hodak, M., Lu, W. & Bernholc, J. Charge transport in DNA nanowires connected to carbon nanotubes. *Phys. Rev. B* **92**, 075429 (2015).
44. Lüpke, F. et al. Local manifestations of thickness-dependent topology and edge states in the topological magnet MnBi<sub>2</sub>Te<sub>4</sub>. *Phys. Rev. B* **105**, 035423 (2022).
45. Landauer, R. Spatial variation of currents and fields due to localized scatterers in metallic conduction. *IBM J. Res. Dev.* **1**, 223–231 (1957).
46. Xiao, Z. et al. Design of atomically precise nanoscale negative differential resistance devices. *Adv. Theory Simul.* **2**, 1800172 (2019).
47. Henkelman, G., Uberuaga, B. P. & Jónsson, H. A climbing image nudged elastic band method for finding saddle points and minimum energy paths. *J. Chem. Phys.* **113**, 9901–9904 (2000).
48. Wrigley, J. et al. Epitaxy of boron nitride monolayers for graphene-based lateral heterostructures. *2D Mater.* **8**, 034001 (2021).
49. Koepke, J. C. et al. Role of pressure in the growth of hexagonal boron nitride thin films from ammonia-borane. *Chem. Mater.* **28**, 4169–4179 (2016).
50. Gorbachev, R. V. et al. Hunting for monolayer boron nitride: optical and Raman signatures. *Small* **7**, 465–468 (2011).
51. Kaniselvan, M., Jeon, Y. R., Mladenovic, M., Luisier, M. & Akinwande, D. Mechanisms of resistive switching in two-dimensional monolayer and multilayer materials. *Nat. Mater.* **24**, 1346–1358 (2025).
52. Britnell, L. et al. Electron tunneling through ultrathin boron nitride crystalline barriers. *Nano Lett.* **12**, 1707–1710 (2012).
53. Längle, M. et al. Defect-engineering hexagonal boron nitride using low-energy Ar<sup>+</sup> irradiation. <https://arxiv.org/html/2404.07166v1> (2024).
54. Kresse, G. & Furthmüller, J. Efficiency of ab-initio total energy calculations for metals and semiconductors using a plane-wave basis set. *Comput. Mater. Sci.* **6**, 15–50 (1996).
55. Perdew, J. P., Burke, K. & Ernzerhof, M. Generalized gradient approximation made simple. *Phys. Rev. Lett.* **77**, 3865–3868 (1996).
56. Giovannetti, G. et al. Doping graphene with metal contacts. *Phys. Rev. Lett.* **101**, 026803 (2008).
57. Grimme, S., Antony, J., Ehrlich, S. & Krieg, H. A consistent and accurate ab initio parametrization of density functional dispersion correction (DFT-D) for the 94 elements H–Pu. *J. Chem. Phys.* **132**, 154104 (2010).
58. Fattbert, J. L. & Bernholc, J. Towards grid-based O(N) density-functional theory methods: Optimized nonorthogonal orbitals and multigrid acceleration. *Phys. Rev. B* **62**, 1713–1722 (2000).
59. Nardelli, M. B., Fattbert, J. L. & Bernholc, J. O(N) real-space method for ab initio quantum transport calculations: application to carbon nanotube–metal contacts. *Phys. Rev. B* **64**, 245423 (2001).
60. Brandbyge, M., Mozos, J.-L., Ordejon, P., Taylor, J. & Stokbro, K. Density-functional method for nonequilibrium electron transport. *Phys. Rev. B* **65**, 165401 (2002).

61. Larade, B., Taylor, J., Mehrez, H. & Guo, H. Conductance, I-V curves, and negative differential resistance of carbon atomic wires. *Phys. Rev. B* **64**, 075420 (2001).

### Acknowledgements

This research was conducted at the Center for Nanophase Materials Sciences, which is a DOE Office of Science User Facility at Oak Ridge National Laboratory. The calculations used resources of the National Energy Research Scientific Computing Center (NERSC), a DOE Office of Science User Facility supported by the Office of Science of the U.S. Department of Energy under Contract No. DE-AC02-05CH11231 using NERSC award BES-ERCAP0031261. We also used resources of the Oak Ridge Leadership Computing Facility, which is a DOE Office of Science User Facility supported under Contract DE-AC05-00OR22725. The Frontier resources were provided through the Innovative and Novel Computational Impact on Theory and Experiment (INCITE) program. D.A. acknowledges the support of the Office of Naval Research (ONR) award #N00014-24-1-2080 and the National Science Foundation (NSF) award #2422934.

### Author contributions

L.L. and P.G. conceptualized and designed the project. L.L., W.L., and E.B. carried out the calculations. D.A. provided experimental insights. L.L. led writing of the manuscript, with contributions from all authors to the analysis of the results and manuscript writing.

### Competing interests

The authors declare no competing interests.

### Additional information

**Supplementary information** The online version contains supplementary material available at <https://doi.org/10.1038/s41699-025-00611-y>.

**Correspondence** and requests for materials should be addressed to Liangbo Liang.

**Reprints and permissions information** is available at <http://www.nature.com/reprints>

**Publisher's note** Springer Nature remains neutral with regard to jurisdictional claims in published maps and institutional affiliations.

**Open Access** This article is licensed under a Creative Commons Attribution 4.0 International License, which permits use, sharing, adaptation, distribution and reproduction in any medium or format, as long as you give appropriate credit to the original author(s) and the source, provide a link to the Creative Commons licence, and indicate if changes were made. The images or other third party material in this article are included in the article's Creative Commons licence, unless indicated otherwise in a credit line to the material. If material is not included in the article's Creative Commons licence and your intended use is not permitted by statutory regulation or exceeds the permitted use, you will need to obtain permission directly from the copyright holder. To view a copy of this licence, visit <http://creativecommons.org/licenses/by/4.0/>.

© The Author(s) 2025